CERN-FASER-CONF-2026-003
20 March 2026

First search for neutrino-induced charm hadrons with FASER's emulsion detector at the LHC

FASER Collaboration

This note presents the first search for charmed-hadron production in high-energy electron and muon neutrino charged-current interactions in the FASERν emulsion–tungsten detector at the LHC. Dedicated tools for reconstructing displaced secondary vertices and classifying decay topologies of charged charm hadrons have been developed and validated using Monte Carlo simulation. A multivariate analysis using Lorentz-invariant kinematical parameters is employed to discriminate charm hadron decays from hadronic interaction backgrounds. The analysis is applied to 40 neutrino interaction candidates identified in 9.5 fb^{-1} of pp collision data at $\sqrt{s} = 13.6$ TeV collected during 2022. A partial unblinding of the data is performed, with a full unblinding of the neutrino candidates expected in the near future.

© 2026 CERN for the benefit of the FASER Collaboration. Reproduction of this article or parts of it is allowed as specified in the CC-BY-4.0 license.

CONTENTS

1. Introduction 1

2. Data and Simulation Samples 2

3. Decay Search Procedure 3
   3.1. Secondary vertex signatures 4
   3.2. In-track Kink Search 5
   3.3. Disconnected Daughter Search 7

4. Event selection 8
   4.1. Basic selection cuts 8
   4.2. Multivariate analysis 11

5. Results 12

6. Conclusions 15

References 16

1. INTRODUCTION

Charm production in neutrino interactions plays an important role in probing both the structure of the nucleon and the dynamics of weak interactions. In charged-current (CC) neutrino interactions, a neutrino can scatter off a valence or sea d quark or a sea s quark, producing a charm quark through the exchange of a W boson. For antineutrinos, no transitions from valence quarks

are allowed; instead, the dominant contribution arises from the transition of a sea $\bar{s}$ into a $\bar{c}$. A subleading contribution comes from the transition of a $\overset{(-)}{d}$ into a $\overset{(-)}{c}$, which is Cabibbo-suppressed due to the smaller CKM matrix element V_{cd}. Once produced, the charm quark hadronizes into charmed hadrons.

The most commonly produced charmed hadrons in neutrino interactions are $D^0, D^\pm, D_s^\pm$ and $\Lambda_c^\pm$. These particles have relatively short lifetimes, with $c\tau$ ranging from $\mathcal{O}(50\ \mu\text{m})$ for Λ_c^+ to 100–300 μm for charmed mesons, leading to displaced decay vertices with different topologies: 1-prong (kink), 3-prong, and 5-prong for charged, and 2-prong, 4-prong, and 6-prong for neutral charmed hadrons.

Charm production in neutrino deep-inelastic scattering (DIS) provides direct access to the strange quark content of the nucleon and has played a central role in global determinations of parton distribution functions (PDFs) [1, 2]. Neutrino-induced charm production also enables detailed tests of charm quark hadronization [3], is uniquely sensitive to heavy-quark mass effects [4, 5], may provide sensitivity to the intrinsic charm component of the nucleon [6, 7], and allows tests of lepton flavour universality in heavy-quark production [8].

Experimentally, charm production in neutrino CC interactions has been investigated through dimuon analyses by CDHS [9], CCFR [10], CHARM [11], CHARM-II [12], NuTeV [13], and CHORUS [3], as well as through invariant mass reconstruction by BEBC [14] and NOMAD [15]. Direct topological observation of displaced charm decay vertices using nuclear emulsion was achieved by E531 [16] (122 candidates) and CHORUS [17] (2013 candidates), while OPERA [18] observed about 50 charm candidates including the first charm production in ν_τCC interactions [19]. To date, no charm production event has been observed in ν_eCC interactions.

The FASER experiment at the LHC, using its emulsion detector (FASERν), extends charm studies into a previously unexplored TeV-energy neutrino interaction regime. The development and validation of tools to detect charm decays also represent an essential step toward the search for τ leptons in ν_τ charged-current interactions, as charm decays constitute an important benchmark for displaced-vertex reconstruction and background characterization.

The FASERν detector, the data and Monte Carlo samples used for this analysis are presented in Sec. 2; the method for identifying secondary vertices is summarized in Sec. 3; Sec. 4 describes the event selection and which kinematical and physical parameters are used to discriminate signal from background secondary vertices; and the results of the event selection is presented in Sec. 5.

2. DATA AND SIMULATION SAMPLES

FASER's emulsion detector (FASERν) is a passive detector that consists of 730 layers of 1.1-mm-thick tungsten plates interleaved with 0.34-mm thick emulsion films [20]. The total mass of FASERν is 1.1 tonnes. The detector has a transverse area of 25 $\times$ 30 cm^2 with respect to the neutrino beam. It is aligned with the line-of-sight and placed in front of the FASER electronic detector, 480 m from the ATLAS pp collision point (IP1). A detailed description of the FASERν detector is provided in Refs. [21, 22].

This analysis uses the second module from the 2022 data-taking period, exposed to 9.5 fb^{-1} of pp collisions at $\sqrt{s} = 13.6$ TeV. Details on data volume, data quality, and neutrino event selection are given in Refs. [23].

Monte Carlo (MC) samples for neutrino interactions are used to develop the decay search, establish selection criteria, and estimate backgrounds. The neutrino fluxes are obtained using the fast neutrino flux simulation presented in Ref. [24], with the prediction for neutrino fluxes from light (π and K) hadrons based on `EPOS-LHC` [25] and from charm hadrons based on `POWHEG+Pythia` [26]. The neutrino interactions were simulated using `GENIE` version 3.4.0 [27] with the `GRV98LO` PDF set.

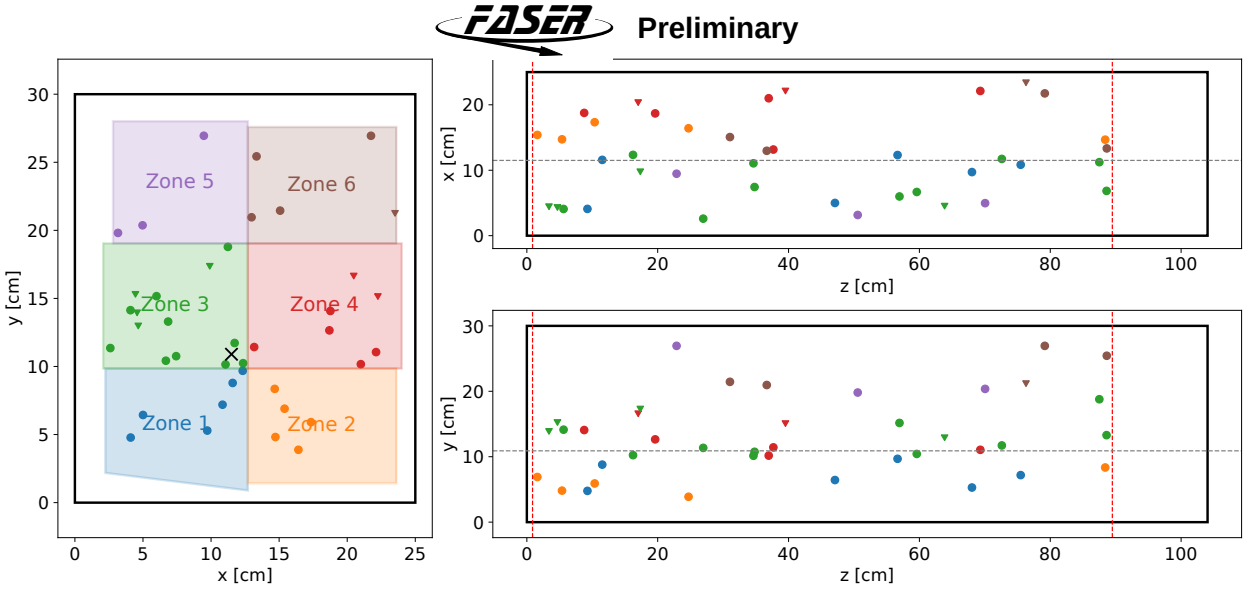


FIG. 1. The location of each neutrino vertex candidate in the detector module, in the xy-, zx- and zy-projected planes. Circles denote ν_μCC candidates and triangles ν_eCC candidates. Coloured polygons show the transverse fiducial volume cuts for each detector zone, and red dashed lines indicate the longitudinal fiducial cuts. The cross in the left plot and the dashed gray lines in the two right plots show the line of sight. The cross in the left plot and the dashed gray lines in the two right plots show the line of sight.

All simulated events are reconstructed using the same reconstruction chain as the data. Corrections are applied to reproduce the hit efficiencies, position and angular resolutions observed in data. The same neutrino event selection criteria used in data are applied to all simulated neutrino flavours. The background and expected signal are normalized to the number of observed neutrino events in data.

In the data, 40 neutrino vertex candidates are identified, of which 33 are ν_μCC and 7 are ν_eCC candidates. The locations of all candidates are shown in Fig. 1. More details about these events can be found in Ref. [28].

The number of primary tracks per neutrino vertex in the data is approximately 9.1 (including the lepton track), corresponding to a total of 364 primary tracks. In the simulated MC sample, the expected number of primaries per vertex is 7.9 (317 primary tracks in total), which is $\approx 15\%$ lower than what is observed. This excess is however within the systematic uncertainty range for different hadronization models for the neutrino interaction.

3. DECAY SEARCH PROCEDURE

The procedure for searching for charm hadrons from neutrino-nucleus CC interactions is shown schematically in Fig. 2. After the primary vertex (the reconstructed ν CC interaction vertex) has been identified, secondary vertices created from interactions or decays of particles produced in the ν CC interaction are searched for. When searching for charged charm hadrons, the secondary vertex search is applied on all primary tracks excluding the lepton track. The secondary vertex search identifies both charm hadron decay vertices and background vertices. The background can be categorized in four different categories:

- Kinks created by multiple Coulomb scattering (MCS), where the daughter and parent track is the same particle

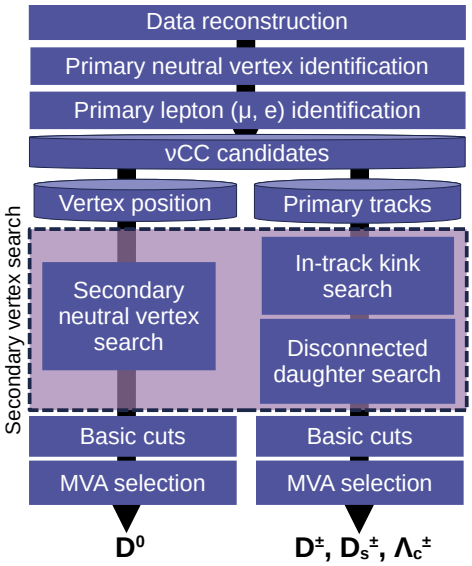


FIG. 2. Schematic of the charm hadron decay search procedure in FASERν. Steps up to neutrino candidate selection are described in Refs. [23, 24].

- fake secondary vertices created by several short tracks inside an electromagnetic (EM) shower
- fake kinks where all the daughter tracks are unrelated background tracks and happen to fulfill the secondary vertex criteria with the parent track (coincidence)
- hadronic interactions of the primary track with the FASERν detector

Note that only when all the daughter tracks are unrelated background tracks, the secondary vertex is classified as a "coincidence" secondary vertex. For the other background categories, a subset of the daughter tracks can sometimes be unrelated tracks.

To extract only charm decay candidates among all the identified secondary vertices, basic kinematical cuts followed by a multivariate analysis (MVA) are applied, as described in Sec. 4.

3.1. Secondary vertex signatures

Charm hadron decays produce several distinct signatures in FASERν, as illustrated in Fig. 3. For charged charm hadrons, a one-prong decay may produce a kink within a reconstructed track, where the upstream part of the track corresponds to the parent track, while the downstream part of the track corresponds to the daughter track (first signature in Fig. 3). A multi-prong decay will create disconnected daughter tracks near the kink point (second signature), or, if the kink angle is large, all daughter tracks are disconnected from the parent track (third signature). The background secondary vertices can also always be categorized in one of these signatures.

For neutral charm hadrons, no visible parent track is present. The daughter tracks therefore form a secondary vertex close to the primary vertex with no parent track. This analysis primarily focuses on the charged secondary vertex search.

The charged secondary vertex search starts with the primary tracks from the neutrino interaction vertex:

- First, a search for kinks is performed using the in-track kink search (Sec. 3.2)
- If a kink is found, the disconnected daughter search (Sec. 3.3) identifies additional daughter

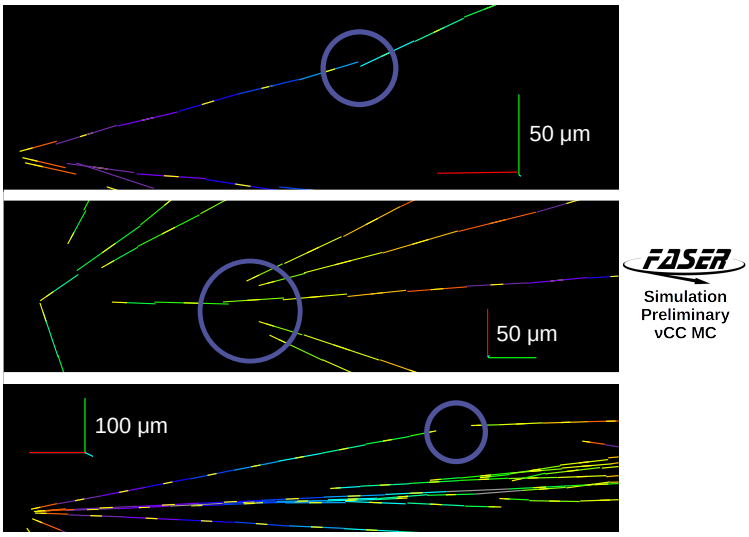


FIG. 3. The three secondary vertex signatures of charged charm hadrons in FASERν, shown with a tilted view with the neutrino interaction to the left. Decay points are highlighted with circles. Yellow segments show base-tracks inside emulsion films; colored lines show extrapolations of the base-tracks into the neighboring tungsten plates. Top: the parent is connected to the daughter and no additional daughter tracks exist, middle: the parent is connected to the daughter and additional disconnected daughters exist, bottom: the parent is disconnected from the daughter(s).

tracks around the detected kink. Additional daughters are expected to be found for the second secondary vertex signature, but not for the first.

- If no kink is found and the track does not leave the reconstructed volume, the disconnected daughter search is applied around the track endpoint to find fully disconnected (third) secondary vertex signatures.

In the simulation samples used for this study, approximately 4% of the identified neutrino vertices are expected to contain a charged charm hadron. Of these, 92% leave a visible parent track, 91% of which have at least one visible daughter track in the reconstructed volume, and 96% of the parent tracks are correctly associated with the primary vertex. The remaining charm hadron decay vertices are the target signal for this analysis. These rates are summarized in Table 1. Note however that this charm production rate depends on the PDF set used, and can be up to twice as high.

The background consists of hadronic interactions of primary hadrons, fake vertices from unrelated background tracks (referred to as "coincidence" secondary vertices in this analysis), large kinks from multiple Coulomb scattering (MCS), and electromagnetic showers.

3.2. In-track Kink Search

The in-track kink search identifies kinks within a single reconstructed track where a charged charm hadron is connected to its daughter track. For each track associated with a neutrino vertex, the angular difference between the upstream and downstream segments is evaluated plate by plate, starting from the plate immediately downstream of the vertex (Fig. 4).

The kink threshold is set based on the position and angular resolutions and the effects of MCS. Using the measured position resolution of 0.3 μm [29], the two-dimensional angular resolution is 0.15 mrad for an arm length of 2.8 mm, corresponding to when three plates upstream of the

TABLE 1. Summary requirements on the secondary vertices in the charged charm search for MC signal. The expected signal counts are normalized to the 40 observed neutrino vertices. The first column shows the expected number of charged charm hadrons, the second column shows the fraction of ν CC interactions with a charged charm secondary vertex, and the third column shows the efficiency of each selection criteria relative to the previous row.

Selection criteria	Expected signal	Fraction of ν CC [%]	Eff. rel. to prev. [%]
Reconstructed ν vertex	40	100.0	
Charged charm produced (truth)	1.6	4.0	4.0
Visible charm track	1.5	3.7	92.2
Visible daughter track	1.3	3.4	91.0
Charm track among primaries	1.3	3.2	96.4

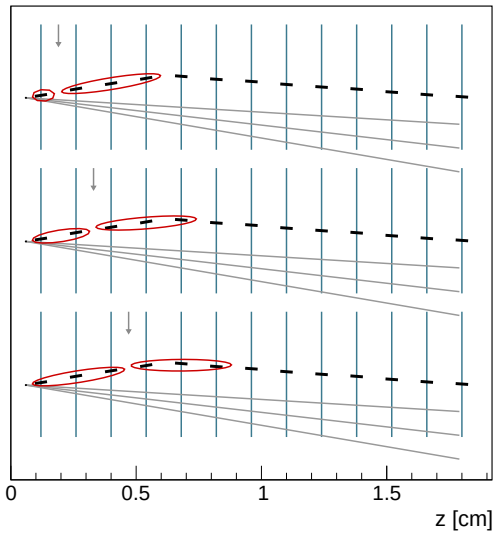


FIG. 4. Schematic of the in-track kink search. The angular difference between upstream and downstream parts is evaluated at each plate. Segments in the red region are used for the angle calculation at the position indicated by the arrow. A kink is identified when the difference exceeds the threshold.

potential kink location are used. When the arm length is shorter, the angular resolution is reduced, and as such, the angular thresholds are set to 1.0, 1.5, and 12 mrad for tracks with three, two, and one upstream segments respectively. This corresponds to approximately four times the angular-difference resolution. For multi-prong secondary vertices, lower thresholds of 0.6, 0.8, and 12 mrad are used initially; if no additional daughters are found, the original thresholds are restored.

The higher threshold for one-prong vertices is motivated by the fact that 96% of the one-prong vertices with kink angles smaller than the original thresholds stated above originate from MCS rather than real interactions. Setting a higher threshold for one-prong secondary vertices removes 18% of the background in MC while only losing 4.5% of signal events.

Kinks are naturally created inside a single particle track due to Multiple Coulomb Scattering. The scattering is inversely proportional to the momentum of the track. However, due to the short lifetime of charm hadrons, the charm track is often short, making the momentum measurement unreliable. Instead, the variables $\Delta\theta_{\mathrm{RMS,\,parent}}$ and $\Delta\theta_{\mathrm{RMS,\,daughter}}$, defined as the root-mean-square of plate-by-plate angular differences, are used. To avoid selecting a kink created by MCS, the kink angle must be at greater than $4\times\Delta\theta_{\mathrm{RMS}}$. Both the resolution-based threshold explained previously and the MCS-based threshold explained here must be independently satisfied. Using this method,

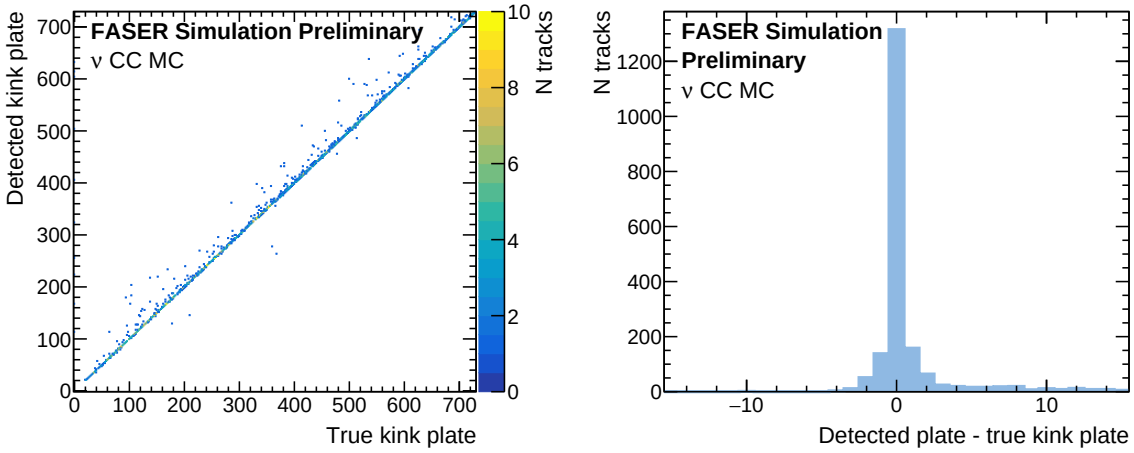


FIG. 5. Detected kink plate versus true kink plate for simulated charged charm hadron tracks (left) and the difference between detected and true kink plate number (right).

most kinks are detected within two plates of the true decay position of the charm hadron in the simulated samples, as shown in Fig. 5.

3.3. Disconnected Daughter Search

After the in-track kink search, the disconnected daughter search is applied to find additional daughter tracks near the kink or track endpoint. Daughter track candidates are selected based on proximity criteria: tracks must start within a maximum transverse distance and within three plates downstream of the parent endpoint. A fitted line is then calculated using the first three segments of the daughter track candidates. This fitted line must satisfy minimum distance and impact parameter requirements relative to the parent track and the reconstructed secondary vertex.

The maximum transverse distance, minimum distance, and impact parameter thresholds dynamically scale with the parent flight length as $\propto F.L.^{-3/2}$. This accounts for the fact that longer-lived (higher-momentum) charm hadrons have smaller MCS-induced uncertainties, allowing for stricter requirements on the minimum distance, impact parameter and transverse distance between parent and daughter tracks.

The free parameters of the search were optimized using a genetic algorithm [30] to maximize the fraction of secondary vertices with both 100% efficiency and purity. Here, efficiency is defined as the fraction of true daughter tracks found for each secondary vertex, while the purity is the fraction of found tracks that are true daughters among the tracks associated with the reconstructed secondary vertex.

A fully reconstructed secondary vertex (100% efficiency and purity) is achieved for 67% of charm decays, while at least one daughter track is found for 87% of cases. The efficiency is approximately uniform across charm hadron species and slightly higher for multi-prong ($\approx 90\%$) than one-prong ($\approx 83\%$) decays.

The initial signal-over-background ratio among all identified secondary vertices is approximately 0.5%. In the data, 293 secondary vertices are found from the 364 primary tracks of the 40 neutrino candidates (254 expected from MC). After removing one-prong vertices with small kink angles, 243 data and 207 MC secondary vertices remain. The composition of secondary vertex signatures is shown in Fig. 6. The excess in the number of primary tracks directly translates to an excess in

secondary vertices. We also see from Fig. 6 that the excess secondary vertices primarily are of the third secondary vertex signature. As described in Sec. 4, this excess background is removed by the basic cuts and therefore does not affect the final results.

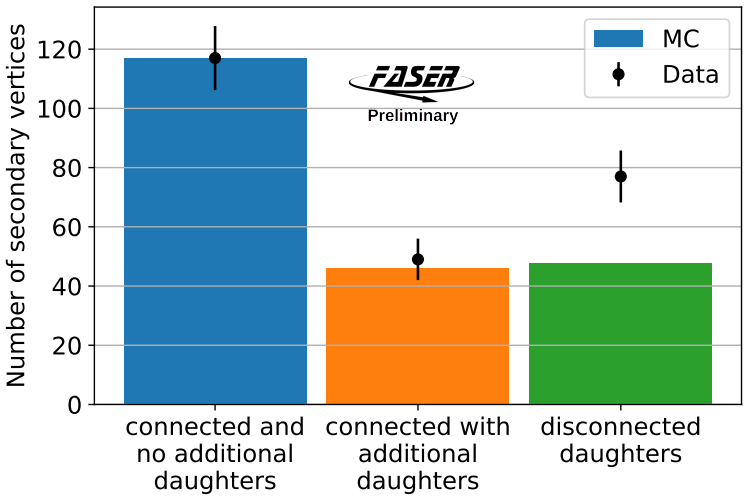


FIG. 6. Comparison of the number of each secondary vertex signature for data and MC. The colored bars show MC, while the dots show the data. The error bars show the statistical uncertainty.

4. EVENT SELECTION

Once secondary vertices have been identified, charm decay candidates are discriminated from background using basic kinematical cuts followed by a MVA. Since charm production has not been probed at $\mathcal{O}(1)$ TeV neutrino energies, the charm hadron kinematics in the simulation may be inaccurate. The selection criteria are therefore designed to primarily use Lorentz-invariant or approximately Lorentz-invariant parameters to minimize dependence on unknown charm hadron kinematics. For all figures and calculations in the following sections, the background and signal is normalized to the observed number of neutrino candidates.

4.1. Basic selection cuts

Since the reconstructed momenta of the daughter tracks are used to discriminate the signal from background secondary vertices, secondary vertices where the momentum reconstruction fails for all the daughter tracks are removed. Additionally, secondary vertices with all daughter tracks shorter than four plates are removed, as such short tracks are typically fake secondary vertices or from electromagnetic showers. These two cuts remove almost all of the excess secondary vertices in the data that were discussed in the previous section and shown in Fig. 6.

The standard deviation of the angles along the parent track, $\sigma(\theta)$, characterizes the track scattering. For charm tracks, this value is close to the emulsion resolution limit ($\sim$0.1 mrad), while background tracks from MCS tend to have larger values. A loose cut of $\sigma(\theta) < 0.45$ mrad is applied.

The scalar sum of transverse momenta of daughter tracks relative to the parent direction, $p_{T,\mathrm{sum}}$, is a Lorentz-invariant parameter with an upper limit of the parent particle mass. Its distribution,

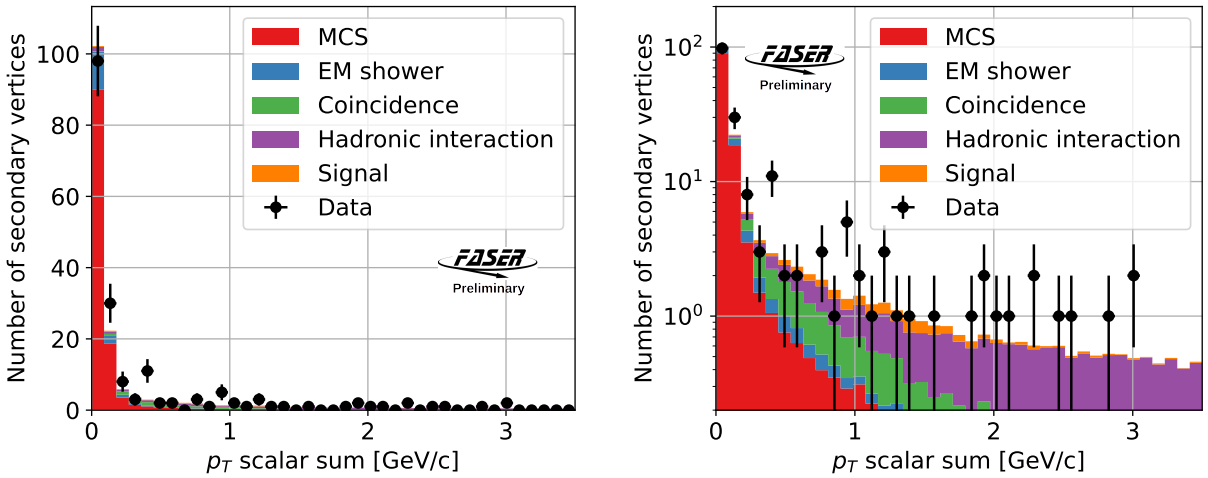


FIG. 7. Data and MC distributions of the scalar sum of transverse momenta of daughter tracks relative to the parent direction, shown with a linear (left) and logarithmic (right) y-axis. The MC signal (orange) and various background contributions are stacked, and the data is overlaid (black points with statistical uncertainties). The different backgrounds are explained in Sec. 3.1.

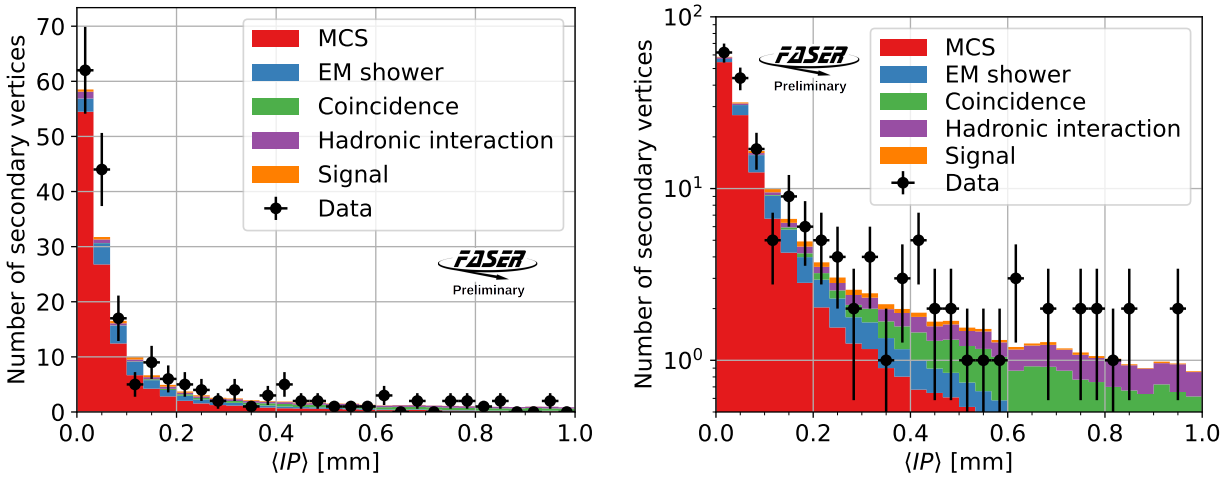


FIG. 8. Data and MC distributions of the mean impact parameter of daughter tracks relative to the primary neutrino vertex, shown with a linear (left) and logarithmic (right) y-axis.

compared between data and MC, is shown in Fig. 7. The momenta of all tracks are calculated using the coordinate method for momentum reconstruction based on multiple Coulomb scattering [31].

The mean impact parameter $\langle IP \rangle$ of daughter tracks relative to the primary neutrino vertex is another Lorentz-invariant parameter. $\langle IP \rangle$ follows an exponential distribution with a characteristic scale of $c\tau$, the lifetime of the charm hadron. The data–MC comparison is shown in Fig. 8.

The ratio $F.L./p_{\text{parent}}$ (flight length over parent momentum) has a typical scale of $c\tau/m$, where m is the mass of the charm hadron. If the parent momentum is not reconstructed or the track has fewer than 10 segments (which is the case for approximately 75% of the parent tracks for both data and MC), twice the sum of longitudinal daughter momenta is used instead as a proxy for the parent momentum. The data–MC comparison is shown in Fig. 9.

The corrected mass m_{corr} [32] estimates the parent mass using daughter track momenta and is

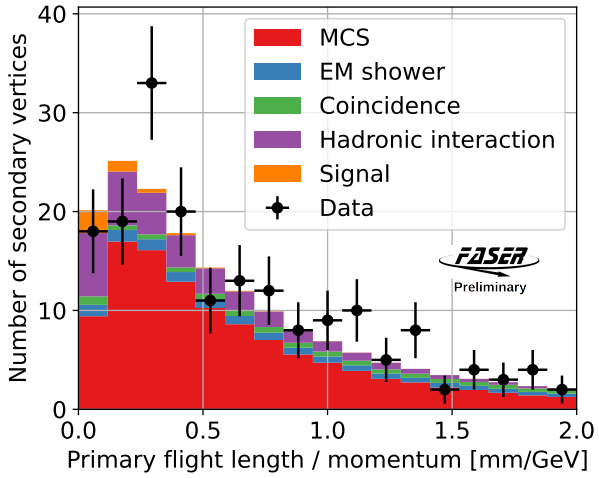


FIG. 9. Data and MC distributions of the flight length divided by the reconstructed parent momentum.

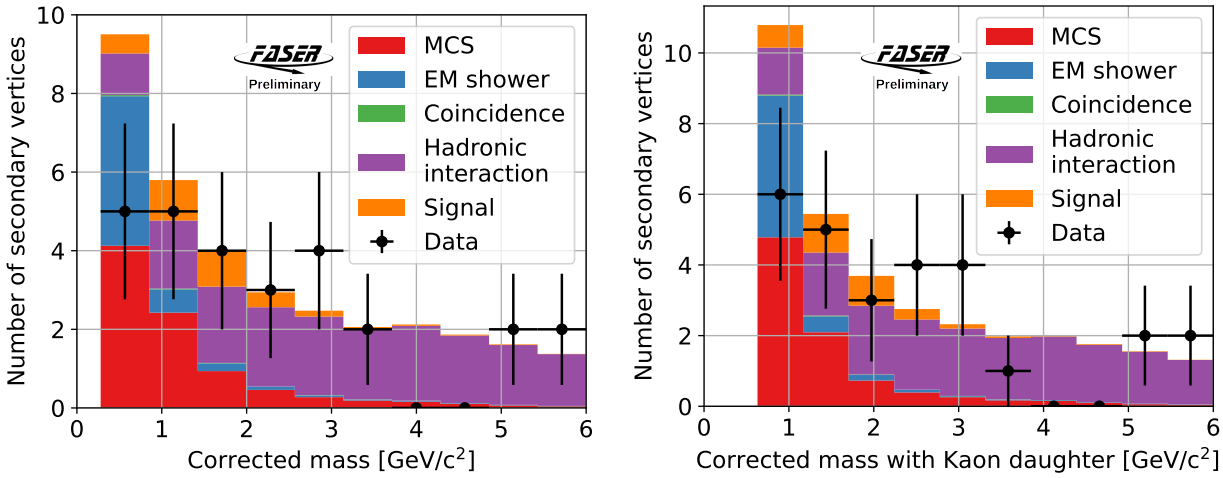


FIG. 10. Data and MC distributions of the corrected mass assuming all daughters have pion masses (left) and with one daughter assigned a kaon mass (right). The mass is only well-defined for secondary vertices with more than one daughter track with reconstructed momentum, and as such, only those secondary vertices are shown. This results in the lower statistics in this figure compared to the other kinematical and physical parameters.

based on assumptions of the invisible neutral decay products. It is defined as:

$$m_{\text{corr}} = \sqrt{m_{\text{vis}}^2 + {p_T^{\text{miss}}}^2} + p_T^{\text{miss}}, \tag{1}$$

where m_{vis} is the visible invariant mass from charged daughters and p_T^{miss} is the missing transverse momentum. Two versions are computed: m_{corr} assuming all daughters have pion masses, and m_{corr}^K where one daughter is assigned a kaon mass (taking the minimum over all permutations). The data–MC comparison is shown in Fig. 10.

The ratio of the vector sum of daughter momenta to the parent momentum is also Lorentz-invariant and provides additional discrimination, and the distributions are shown in Fig. 11. Note that this parameter is only defined when both the parent and the momentum of at least one

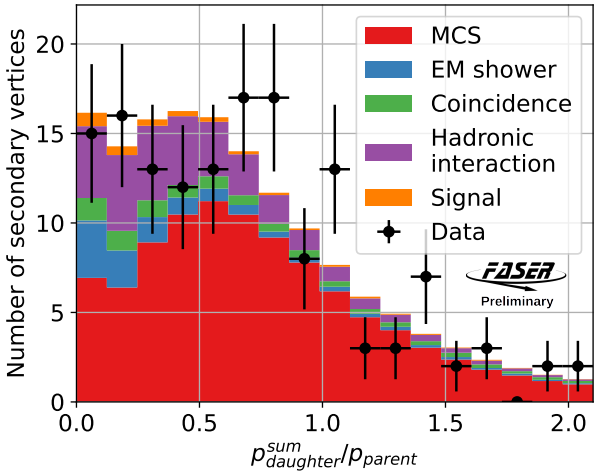


FIG. 11. Data and MC distributions of the ratio between the vector sum of daughter track momenta and the parent track momentum.

TABLE 2. Cut flow for the basic selection cuts. The fraction of MC background, MC signal, and data secondary vertices remaining after each cumulative cut is shown relative to the initial count after the small-kink removal.

Selection criteria	Background left (%)	Signal left (%)	Data left (%)
No cut	100.0	100.0	100.0
Longest daughter $\geq$ 4 plates	86.9	99.6	81.5
$\sigma(\theta) < 0.45$ mrad	84.1	98.9	78.2
Reconstructed daughter momentum	60.2	97.6	54.7
p_T sum $\leq$ 3.4 GeV	53.1	93.4	48.6
$\langle IP \rangle$ relative to primary $\leq$ 1000 μm	47.1	91.5	41.6
Primary L/p $\leq$ 0.4 mm/GeV	24.2	84.9	22.6
Corrected mass $\leq$ 5 GeV	24.2	84.9	22.6

daughter track have been reconstructed. No requirement on the length of the parent track is used.

Overall, the agreement between the data and MC distributions for these kinematical and physical parameters is good.

The basic cuts on each parameter described in this section, as well as the cut flow and remaining number of secondary vertices in the MC signal, MC background, and data are given in Table 2. The number of secondary vertices rejected by the basic cuts is slightly higher for the data than MC, corresponding to the rejection of the excess data. This is also evident from Fig. 12, where the number of each secondary vertex signature in data and MC are compared after the basic cuts. The excess of disconnected daughter vertices seen before cuts (attributable to the $\approx$15% excess in observed primary tracks per vertex relative to MC) is removed by the basic cuts.

4.2. Multivariate analysis

After the basic cuts, a machine learning classifier based on an explainable boosting machine (EBM) [33] is used. The EBM is a generalized additive model where the MVA score output g for

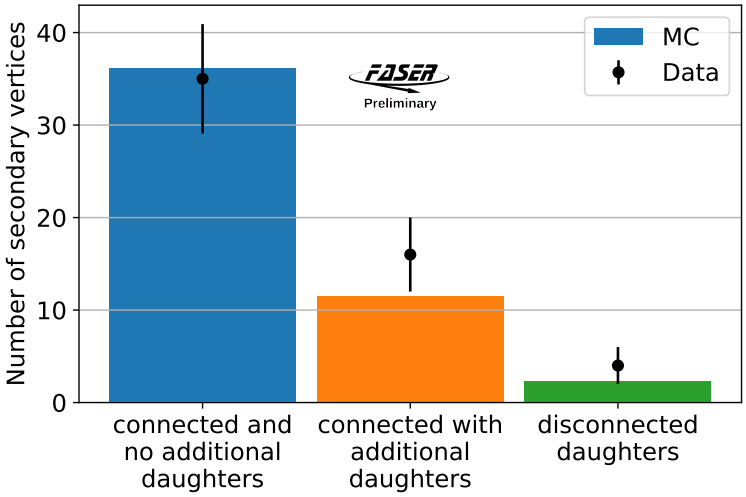


FIG. 12. Data and MC counts of the three secondary vertex categories after basic cuts. Lighter bars show MC with statistical uncertainties; darker bars show data.

an input with parameter values $x_1, ..., x_N$ is given by:

$$g(x_1, \ldots, x_N) = \beta_0 + \sum_{i=1}^{N} f_i(x_i) + \sum_{i<j} f_{i,j}(x_i, x_j), \tag{2}$$

where $g \approx 1$ indicates signal-like and $g \approx 0$ background-like vertices, β_0 is a trainable parameter and $f_i, f_{i,j}$ are trainable functions. The model's additive structure makes it inherently interpretable [34], which is important to reduce overfitting, and particularly useful given the uncertainties in the simulation for charm production at TeV energies. Empirically, it has been shown that the EBM has a similar performance as boosted decision trees.

The EBM is trained on eight parameters: the number of daughter tracks, the number of daughter tracks with reconstructed momentum, $p_{T,\text{sum}}$, $\langle IP \rangle$, $F.L./p_{\text{parent}}$, m_{corr}, m^K_{corr}, and the daughter-to-parent momentum ratio. 80% of events are used for training and 20% for testing. The signal training sample is augmented with charm hadrons from all neutrino energies (not only those passing vertex selection) to increase statistics, exploiting the approximate Lorentz invariance of the training variables. During training, signal weights are rescaled to improve the model's sensitivity to the rare signal class. The MVA performance is shown in Fig. 13. At a threshold of 0.735, corresponding to a 1:1 signal-to-background ratio, the signal efficiency is 54% and the background survival rate is 0.99%. From the signal-to-background ratio curve in Fig. 13, we see that almost a pure signal is expected for MVA scores above 0.95.

5. RESULTS

A summary of all selection criteria and their cumulative efficiencies for the signal is shown in Table 1. The charm identification efficiency is independent of neutrino flavour and approximately independent of charm momentum, though slightly higher for high-momentum charm hadrons.

The number of secondary vertices expected for the signal, the background, and the secondary vertices observed in data are given in Table 3. As stated in Sec. 3.3, there is an excess in the number of primary tracks in the data compared to the MC, resulting in an excess in the number of secondary vertices that are reconstructed. As observed in Fig. 6, this excess is primarily composed

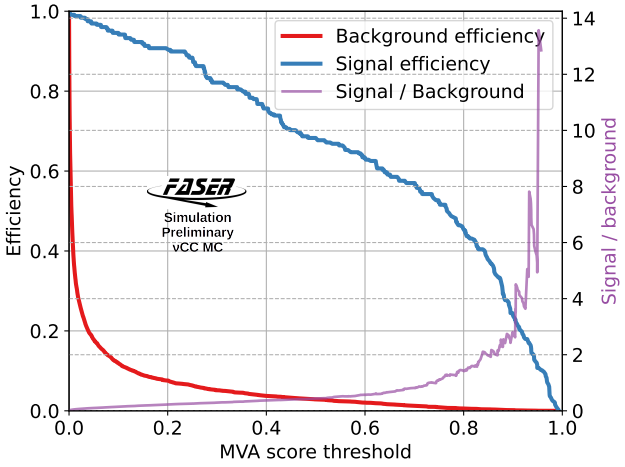


FIG. 13. The signal efficiency (blue), background survival rate (red), and signal-to-background ratio (purple) as a function of the MVA threshold for the MC samples.

TABLE 3. Summary cut flow for the charged charm search for MC signal, MC background, and the number of secondary vertices observed in the data. The expected signal and background secondary vertex counts are normalized to the 40 observed neutrino vertices. A detailed cut flow for the basic cuts are given in Table 2.

Selection criteria	Expected signal	Expected background	Data
Secondary vertex reconstructed	1.1	253	293
Small kink cut	1.1	206	243
Basic cuts	0.92	50	55

of secondary vertices where all the daughter tracks are disconnected, and therefore mainly come from low-momentum primary tracks. After applying the basic cuts, this excess background is removed, as can be seen in Fig. 12. The data–MC agreement after the basic cuts is therefore good, with approximately 51 secondary vertices expected in MC and 55 secondary vertices observed among the 40 neutrino vertices.

In order to avoid biasing future analyses, a full unblinding is not performed. Instead, only the first neutrino candidates published in Ref. [29] are unblinded and passed through the MVA. In total, there are 17 secondary vertices from these neutrino candidates which pass the basic cuts. The MVA scores for these secondary vertices are shown in Fig. 14, together with the MC MVA score distribution. The data–MC agreement is relatively good, though there are two secondary vertices MVA scores above 0.5. Event displays of these two secondary vertices are shown in Figs. 15 and 16.

The event with a MVA score of 0.87 is a track with a kink, with three additional short daughter tracks. A visual inspection revealed that there was an EM shower upstream that overlapped with the kink by coincidence, adding the additional fake disconnected daughters to the secondary vertex. The event display for this event is shown in Fig. 15. This makes it unlikely to be a charm decay. No automated tool currently exists to reject such backgrounds, but is currently being developed and will reduce this background in future analyses.

The secondary vertex with the second highest MVA score had a value of 0.67. A visual inspection revealed that it is a high-momentum hadronic track with either a decay or a secondary interaction, creating secondary hadrons and EM showers. The event display for this event is shown in Fig. 16. At the current stage of the analysis however, it cannot yet be concluded whether this is a charm hadron decay or a hadronic interaction. This is because the MVA score of this secondary vertex is still in the background-dominated region, and some improvements to the treatment of systematics

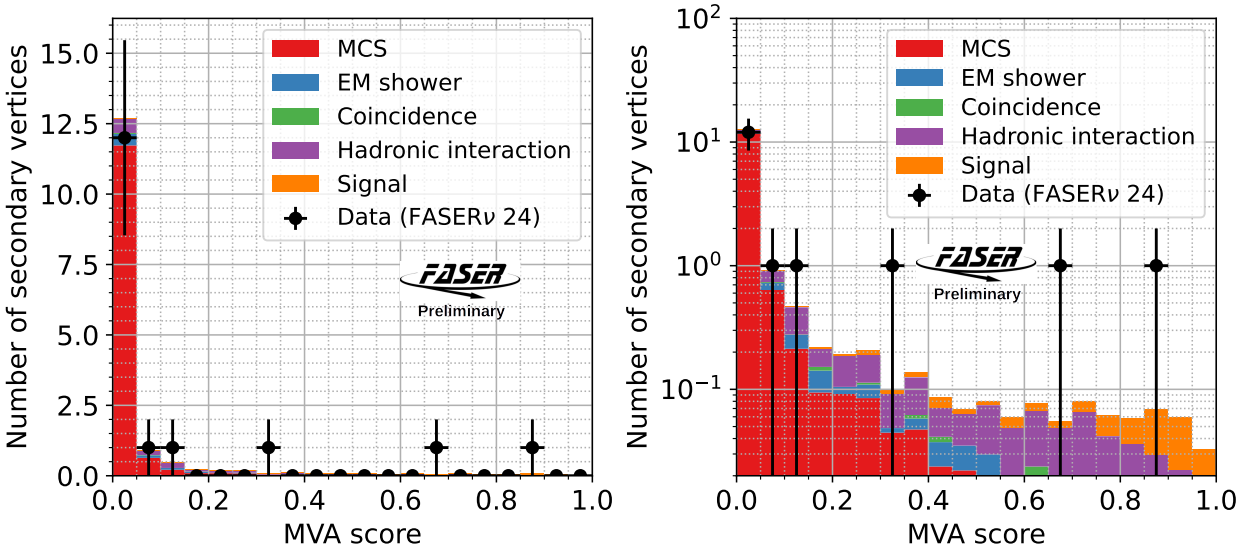


FIG. 14. Left: MVA score distribution for signal and background (stacked) in the test sample. The distributions have been normalized to be equal to the number of expected secondary vertices among the first neutrino candidates in Ref. [29]. Right: same as the left figure with a logarithmic y-axis.

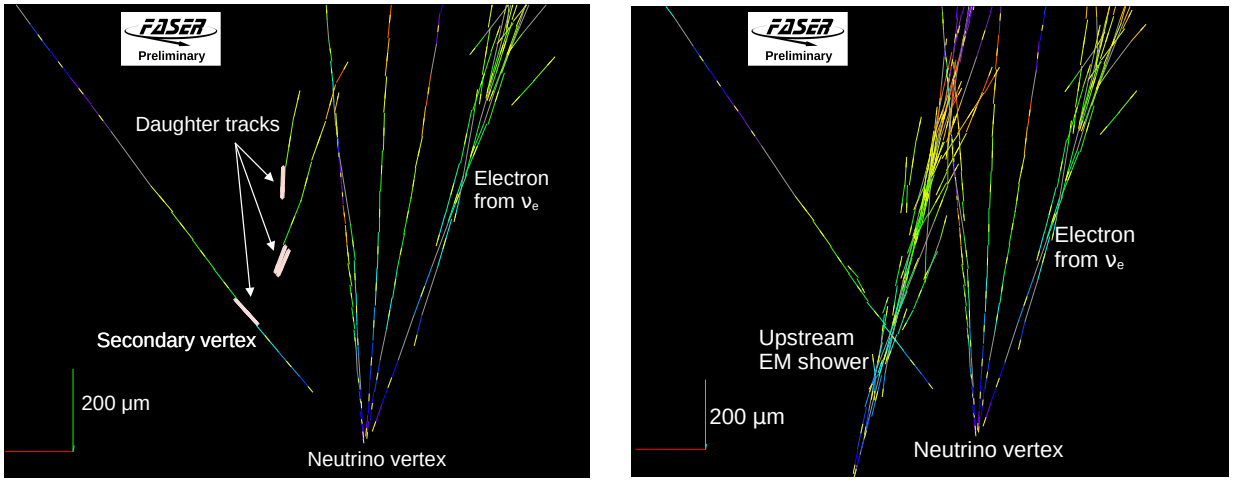


FIG. 15. Event display with a tilted view of the candidate with the highest MVA score (0.87) among the secondary vertices from the neutrino candidates in Ref. [29]. Left: the primary neutrino vertex and its primaries, and the secondary vertex and the daughter tracks found by the secondary vertex search, where the first segment of each daughter track is highlighted. Right: the same event display with the upstream EM shower of which the disconnected daughters are a part of.

still needs to be done in order to better understand the background.

Overall, these results show that the agreement between data and MC are generally good, though some improved treatment of systematics is still needed. This will be completed in the near future, which will be followed by a full unblinding of the MVA score distribution of the secondary vertices.

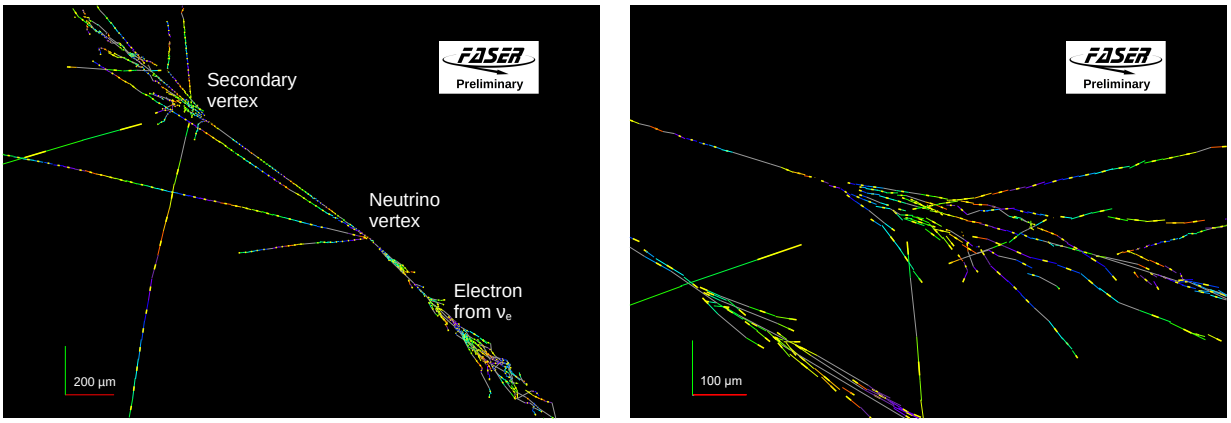


FIG. 16. Event display of the candidate with the second highest MVA score (0.67) among the secondary vertices from the neutrino candidates in Ref. [29]. Left: the neutrino interaction viewed from the beam view, with the secondary vertex at the top. Right: a zoomed-in and tilted display of the same secondary vertex, showing the hadron tracks and EM shower.

6. CONCLUSIONS

This note presents the first ever search for charged charm hadron production from electron and muon neutrino interactions in the TeV energy scale. Seven electron-neutrino interaction candidate events and thirty three muon-neutrino interaction candidate events from the FASERν tungsten-emulsion detector, exposed to 9.5fb^{-1} of pp collisions, are used to search for these charged charm hadrons.

A dedicated decay vertex tool has been developed. The identified secondary vertices are then passed through basic cuts on the kinematical and physical parameters, followed by a multivariate analysis to discriminate signal decay vertices from background secondary vertices. To avoid biasing the selection cuts against the charm kinematics, primarily Lorentz-invariant parameters are used.

We observe generally good agreement between data and MC for the distributions of physical and kinematical parameters, within statistical uncertainties. Some excess in the number of background secondary vertices are seen, but these secondary vertices are rejected by the basic cuts and therefore do not affect the final results. Lastly, a partial unblinding of the MVA scores, using only the secondary vertices from the neutrino vertices presented in Ref. [29], were computed and compared to the MC distribution. The two secondary vertices with the highest MVA scores were inspected.

At the current stage of the analysis, it cannot yet be concluded whether the secondary vertices with high MVA scores are charm hadron decays or hadronic interactions. Further studies will allow better understanding and reduction of background, with improved treatment of systematics. This will be followed by a full unblinding of the MVA score distribution for the remaining FASERν neutrino candidates in the near future, corresponding to a four-fold increase in statistics. This will pave the way for the first ever observation of neutrino-induced charm production at the TeV energy scale.

This analysis is an important milestone which marks the beginning of detailed studies of the hadronic system of neutrino-nucleus interactions in an energy regime that has never been probed before. In particular, charm hadron production from neutrino interactions plays a fundamental role in improving our understanding of both the structure of the nucleon and the mechanism of

the weak force.

---

[1] J. M. Cruz-Martinez, M. Fieg, T. Giani, P. Krack, T. Mäkelä, T. R. Rabemananjara, and J. Rojo, "The LHC as a Neutrino-Ion Collider," *Eur. Phys. J. C* **84** (2024) no. 4, 369, arXiv:2309.09581 [hep-ph].

[2] F. Faura, S. Iranipour, E. R. Nocera, J. Rojo, and M. Ubiali, "The Strangest Proton?," *Eur. Phys. J. C* **80** (2020) no. 12, 1168, arXiv:2009.00014 [hep-ph].

[3] **CHORUS** Collaboration, "Leading order analysis of neutrino induced dimuon events in the CHORUS experiment," *Nucl. Phys. B* **798** (2008) 1–16, arXiv:0804.1869 [hep-ex].

[4] S. Forte, E. Laenen, P. Nason, and J. Rojo, "Heavy quarks in deep-inelastic scattering," *Nucl. Phys. B* **834** (2010) 116–162, arXiv:1001.2312 [hep-ph].

[5] E. L. Berger, J. Gao, C. S. Li, Z. L. Liu, and H. X. Zhu, "Charm-Quark Production in Deep-Inelastic Neutrino Scattering at Next-to-Next-to-Leading Order in QCD," *Phys. Rev. Lett.* **116** (2016) no. 21, 212002, arXiv:1601.05430 [hep-ph].

[6] S. J. Brodsky, P. Hoyer, C. Peterson, and N. Sakai, "The Intrinsic Charm of the Proton," *Phys. Lett. B* **93** (1980) 451–455.

[7] **NNPDF** Collaboration, R. D. Ball, A. Candido, J. Cruz-Martinez, S. Forte, T. Giani, F. Hekhorn, K. Kudashkin, G. Magni, and J. Rojo, "Evidence for intrinsic charm quarks in the proton," *Nature* **608** (2022) no. 7923, 483–487, arXiv:2208.08372 [hep-ph].

[8] D. Guadagnoli and P. Koppenburg, "Lepton Flavor Violation and Lepton Flavor Universality Violation in b and c Decays," *Ann. Rev. Nucl. Part. Sci.* **73** (2023) 1–21, arXiv:2207.01851 [hep-ph].

[9] H. Abramowicz *et al.*, "Experimental Study of Opposite Sign Dimuons Produced in Neutrino and anti-neutrinos Interactions," *Z. Phys. C* **15** (1982) 19.

[10] S. A. Rabinowitz *et al.*, "Measurement of the Strange Sea Distribution using Neutrino Charm Production," *Phys. Rev. Lett.* **70** (1993) 134–137.

[11] **CHARM** Collaboration, "Experimental Study of Opposite Sign and Same Sign Dimuon Events Produced in Wide Band Neutrino and Anti-neutrino Beams," *Phys. Lett. B* **107** (1981) 241.

[12] **CHARM II** Collaboration, "Leading order QCD analysis of neutrino induced dimuon events," *Eur. Phys. J. C* **11** (1999) 19–34.

[13] **NuTeV** Collaboration, "Precise Measurement of Dimuon Production Cross-Sections in ν_μ Fe and $\bar{\nu}_\mu$ Fe Deep Inelastic Scattering at the Tevatron.," *Phys. Rev. D* **64** (2001) 112006, arXiv:hep-ex/0102049.

[14] **Big Bubble Chamber Neutrino** Collaboration, "Study of D*+ and search for D**0 production by neutrinos in BEBC," *Z. Phys. C* **68** (1995) 43–46.

[15] **NOMAD** Collaboration, "A Precision Measurement of Charm Dimuon Production in Neutrino Interactions from the NOMAD Experiment," *Nucl. Phys. B* **876** (2013) 339–375, arXiv:1308.4750 [hep-ex].

[16] **Fermilab E531** Collaboration, "Cross Sections for Neutrino Production of Charmed Particles," *Phys. Lett. B* **206** (1988) 375–379.

[17] A. Kayis-Topaksu *et al.*, "Measurement of charm production in neutrino charged-current interactions," *New J. Phys.* **13** (2011) 093002, arXiv:1107.0613 [hep-ex].

[18] **OPERA** Collaboration, "Procedure for short-lived particle detection in the OPERA experiment and its application to charm decays," *Eur. Phys. J. C* **74** (2014) no. 8, 2986, arXiv:1404.4357 [hep-ex].

[19] **OPERA** Collaboration, "First observation of a tau neutrino charged current interaction with charm production in the OPERA experiment," *Eur. Phys. J. C* **80** (2020) no. 8, 699, arXiv:1912.11012 [hep-ex].

[20] A. Ariga, T. Ariga, G. De Lellis, A. Ereditato, and K. Niwa, *Nuclear Emulsions*, pp. 383–438. 2020.

[21] **FASER** Collaboration, H. Abreu *et al.*, "The FASER detector," *JINST* **19** (2024) no. 05, P05066, arXiv:2207.11427 [physics.ins-det].

[22] **FASER** Collaboration, "Reconstruction and performance evaluation of FASER's emulsion detector at the LHC," *JINST* **20** (2025) no. 12, P12018, arXiv:2504.13008 [physics.ins-det].

[23] **FASER** Collaboration, "Updated results of high-energy electron and muon neutrino interactions with FASER's emulsion detector at the LHC,". https://cds.cern.ch/record/2927714.

[24] **FASER** Collaboration, H. Abreu *et al.*, "Neutrino rate predictions for FASER," *Phys. Rev. D* **110** (2024) no. 1, 012009, arXiv:2402.13318 [hep-ex].

[25] T. Pierog, I. Karpenko, J. M. Katzy, E. Yatsenko, and K. Werner, "EPOS LHC: Test of collective hadronization with data measured at the CERN Large Hadron Collider," *Phys. Rev. C* **92** (2015) no. 3, 034906, arXiv:1306.0121 [hep-ph].

[26] S. Frixione, P. Nason, and C. Oleari, "Matching NLO QCD computations with Parton Shower simulations: the POWHEG method," *JHEP* **11** (2007) 070, arXiv:0709.2092 [hep-ph].

[27] C. Andreopoulos, C. Barry, S. Dytman, H. Gallagher, T. Golan, R. Hatcher, G. Perdue, and J. Yarba, "The GENIE Neutrino Monte Carlo Generator: Physics and User Manual," arXiv:1510.05494 [hep-ph].

[28] **FASER** Collaboration, "Updated candidate events and cross section measurements of high-energy electron and muon neutrino interactions with FASER's emulsion detector at the LHC,". https://cds.cern.ch/record/2956166.

[29] **FASER** Collaboration, "First Measurement of νe and $\nu\mu$ Interaction Cross Sections at the LHC with FASER's Emulsion Detector," *Phys. Rev. Lett.* **133** (2024) no. 2, 021802, arXiv:2403.12520 [hep-ex].

[30] A. F. Gad, "Pygad: An intuitive genetic algorithm python library," *Multimedia Tools and Applications* (2023) 1–14.

[31] **FASER** Collaboration, "Momentum Measurement of Charged Particles in FASER's Emulsion Detector at the LHC," tech. rep., 2, 2026. arXiv:2602.17575 [physics.ins-det].

[32] **SLD** Collaboration, "A Measurement of R(b) using a vertex mass tag," *Phys. Rev. Lett.* **80** (1998) 660–665, arXiv:hep-ex/9708015.

[33] H. Nori, S. Jenkins, P. Koch, and R. Caruana, "Interpretml: A unified framework for machine learning interpretability." Arxiv preprint, 2019. https://arxiv.org/abs/1909.09223.

[34] Y. Lou, R. Caruana, and J. Gehrke, "Intelligible models for classification and regression," in *Proceedings of the 18th ACM SIGKDD international conference on Knowledge discovery and data mining*, pp. 150–158. 2012.